(Received 16 May 2024, Accepted 22 July 2024, Scheduled 1 August 2024)

An Adjustable Sensorless Strategy for Start-up and Low-to-Medium Speed with Six-Phase SRM

Jianfei Sun[1], Zebin Yang[1], and Xiaodong Sun[2,*]

[1] School of Electrical and Information Engineering, Jiangsu University, Zhenjiang 212013, China
[2] Automotive Engineering Research Institute, Jiangsu University, Zhenjiang 212013, China

ABSTRACT: To address challenges such as low starting torque and inaccurate position estimation in traditional sensorless control methods for switched reluctance motors (SRMs), this paper proposes a sensorless control strategy suitable for the startup and low-to-medium speed operation of multiphase SRMs. Firstly, an improved inductance calculation model for the pulse injection region is proposed based on the electromagnetic characteristics of SRM. Secondly, leveraging the results of the inductance model calculation, a three-phase commutation rule is designed to enhance the starting capability. Lastly, an adaptive angle tuning (AAT) module is devised to improve the phase commutation width, and the pulse injection region is optimized through a dynamic inductance threshold method. The efficacy of the proposed method was validated through simulations conducted on a prototype six-phase 12/10 SRM.

1. INTRODUCTION

Nowadays, SRMs have garnered considerable attention from researchers both domestically and internationally due to their inherent advantages, including simple structure, wide speed range, high reliability, and strong fault tolerance. As a result, SRMs are considered favorable competitors in the future development of magnet-free motors [1, 2]. In recent years, SRMs have found applications in the fields of electric vehicles [3] and the aerospace industry [4]. The operation of SRMs relies on real-time rotor position information, which is typically obtained through the position or velocity sensors. However, sensor measurements are susceptible to environmental influences such as high temperatures, high pressures, and humidity, which can affect measurement accuracy and reduce the reliability of the control system [5]. Therefore, the research on sensorless techniques is highly necessary.

In the research on sensorless control, methods based on lookup tables [6], state observers [7], neural networks [8], and others have been developed. The implementation of these methods typically requires a significant amount of sample data for constructing prior models, involves complex computation processes, demands high computational capabilities from digital processors, and necessitates substantial memory allocation [9]. To unleash processor performance and achieve rapid estimation of position information, a feature-based position detection method grounded on electromagnetic characteristics has been proposed [10]. Sensorless techniques based on feature position detection encompass methods such as current slope estimation [11], inductance slope estimation [12], reluctance estimation [13], and inductance threshold estimation [14]. However, the accuracy of feature position estimation is significantly affected by magnetic saturation phenomena, and substantial errors exist in flux integration at low speeds, necessitating further refinement.

Additionally, with the application of robust control theory to SRM, sliding mode control has seen further development. In [15], a sliding mode observer position estimation method based on an inductance model is proposed, enabling rapid estimation of the rotor position. [16] presents an adaptive gain super twisting sliding mode observer (AGST-SMO) for SRM drive with an enhanced transient behaviour. In [17], the derivative of the instantaneous inductance is used as a function error to improve the estimation accuracy of the sliding mode observer. Building on this, sliding mode theory has also been applied to the design of speed controllers to accelerate the system response time [18, 19].

The variation in flux linkage can reflect positional information [20], and this characteristic has been used by some researchers for rotor position estimation. In [21], the rotor position is estimated by comparing the phase flux linkage with the stored motor flux linkage characteristics to obtain symmetrical rotor information. In [22], a flux linkage model is established using a polynomial of the flux linkage, and the rotor position information is discretized for estimation. In [23], a flux linkage model is developed using Fourier series, and virtual Hall signals are obtained by real-time comparison with the actual flux linkage to estimate the rotor position. Flux estimation methods often require predefined or real-time calculation of digital models of flux, which imposes significant computational costs on the controller and adversely affects response capabilities.

The pulse injection method [24] is widely applied in position estimation during the startup and low-to-medium speed phases of SRMs. In [25], a method based on idle phase injection and current amplitude comparison is proposed to achieve position estimation during startup and low-speed states. However, in

* Corresponding author: Xiaodong Sun (xdsun@ujs.edu.cn).

this method, the pulse injection region is fixed. Typically, a fixed injection pulse region can lead to additional switching losses and a delay in the demagnetization time of the windings, which should be minimized whenever possible. In [26], a comparative analysis of different methods and regions for pulse injection is conducted to determine the appropriate pulse signal. In [27], a dual inductance threshold positioning method based on pulse injection is proposed, utilizing the zero-crossing point of the inductance slope to determine the aligned position. However, the method lacks consideration for the impact of magnetic saturation phenomena on position estimation, resulting in less accuracy during startup and under high-load conditions. Ref. [28] improves a sensorless control method under startup and high-load conditions by considering the effects of magnetic saturation. It achieves unsaturated inductance reconstruction and performs inductance coordinate transformation to obtain position information. However, this method does not account for the influence of winding switching angles, and single-phase startup schemes may not offer significant starting torque. To address the sensorless high-speed operation of SRMs, the reluctance estimation method [29] and inductance decoupling method [30] have been used to reconstruct rotor information at high speeds.

The adjustment of winding switching angles is essential for optimizing torque performance, and it should be continuously adapted according to changes in operating conditions. In [31], an analysis of the responsiveness of the commutation angle to the excitation current is conducted, indicating that the turn-on angle should advance with increasing speed to prevent phase current loss of control. In [32], a general theory of optimal turn-on angle for average torque control is introduced. In [33], torque generation capability is enhanced through adjustments to the SRM commutation strategy. Additionally, [34] proposes a torque error regulator based on proportional coefficient adjustment and the phase current detector to dynamically adjust the winding switching angles. However, this approach does not take into account the inherent electromagnetic characteristics of SRMs, which is clearly unsuitable when applying sensorless technologies.

Drawing inspiration from the aforementioned research, this paper proposes a sensorless control strategy for the startup and low-to-medium speed operation of a six-phase SRM based on the pulse injection method. The aim is to enhance position estimation accuracy and motor startup capability. By adjusting the winding switching angles online and optimizing the pulse injection region, sensorless control of the six-phase SRM is achieved.

The remainder of this paper is organized as follows. Section 2 introduces the proposed sensorless startup strategy. Section 3 analyzes the adaptive angle tuning process and streamlines the pulse injection region. Section 4 presents the simulation results, and Section 5 summarizes the entire paper.

2. PROPOSED SENSORLESS STARTUP METHOD

Generally, SRMs require high torque during startup. Therefore, the torque output capability at startup and accurate initial position estimation are key focuses of research on sensorless control for SRMs. In this section, we utilize the pulse injection method for initial position estimation and propose a sensorless startup strategy based on the inductance threshold of characteristic positions. This strategy facilitates the transition from startup to low-speed operation.

2.1. Unsaturated Inductance Calculation Model

In general, power units for SRMs commonly use asymmetric half-bridge (AHB) circuits rather than H-bridge circuits. This choice is because each phase winding of an SRM is controlled independently, requiring only unidirectional current flow to create a magnetic field that aligns the rotor. From cost and efficiency perspectives, AHB circuits use fewer switch devices, thereby reducing costs. Compared to H-bridge circuits which control bidirectional current, AHB circuits result in lower switching and conduction losses, simplifying thermal management.

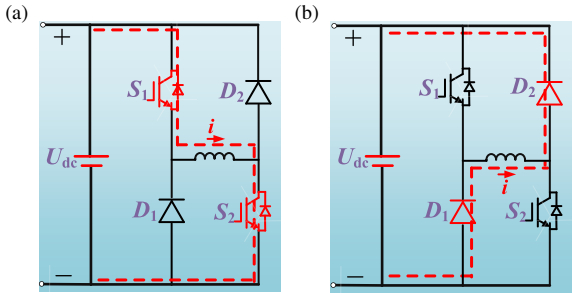

FIGURE 1. Asymmetric half-bridge equivalent circuit. (a) Excitation state. (b) Demagnetization state.

Figure 1(a) illustrates the equivalent circuit of the AHB in the excitation state, where both switches in the circuit are simultaneously closed to form a loop. Fig. 1(b) depicts the equivalent circuit of the AHB in the demagnetization state, where the switches are open, and a loop is formed through the diodes. During the excitation and demagnetization periods of the phase windings, the voltage balance equations can be represented as:

$$U_{dc} - 2V_T = Ri_{on} + \frac{d\varphi(i,\theta)}{dt} \tag{1}$$

$$-U_{dc} - 2V_D = Ri_{off} + \frac{d\varphi(i,\theta)}{dt} \tag{2}$$

where U_{dc}, R_{ph}, i, θ, V_T, V_D, and $\varphi(i,\theta)$ represent the DC bus voltage, the equivalent resistance of the phase winding, phase current, rotor position, conduction voltage drop across the switch, conduction voltage drop across the diode, and flux linkage, respectively. The time derivative of the flux linkage can be decomposed into partial derivatives with respect to angle and phase current, as follows:

$$\frac{d\varphi(i,\theta)}{dt} = \frac{\partial\varphi(i,\theta)}{\partial\theta}\omega + \frac{\partial\varphi(i,\theta)}{\partial i}\frac{di}{dt} \tag{3}$$

The partial derivative with respect to angle in (3) represents the back electromotive force (EMF), which counteracts the DC bus voltage. The partial derivative with respect to the current

TABLE 1. Rules of the initial phase commutation.

Region	I	II	III	IV	V	VI
Driving phase	E, F, A	F, A, B	A, B, C	B, C, D	C, D, E	D, E, F

consists of the slope of the φ-i curve and the current derivative. Typically, the slope of φ-i curve is defined as the incremental inductance, denoted as:

$$L_{inc}(i,\theta) = \frac{\partial \varphi(i,\theta)}{\partial i} \tag{4}$$

It is important to note that the incremental inductance $L_{inc}(i,\theta)$ may not always be identical to the self-inductance $L(i,\theta)$. In [35], the inductance is analyzed by dividing it into unsaturated and saturated regions, leading to the conclusion that L_{inc} equals L only in the unsaturated region of the inductance. Therefore, certain sensorless position estimation strategies based on the L inductance model may exhibit significant position estimation errors under magnetic saturation conditions. The back EMF can be further expressed as:

$$\frac{\partial \varphi(i,\theta)}{\partial \theta}\omega = i\omega \frac{\partial L_{inc}(i,\theta)}{\partial \theta} \tag{5}$$

In this study, the startup state consists of two parts: static initial position estimation and high-frequency pulse injection before startup stabilization. In this process, the values of ω and i are very small, even zero. Therefore, the contribution of back EMF during the startup stage is relatively low and can be omitted for computational simplicity.

Based on the analysis of (1) to (5), the calculation model for incremental inductance can be expressed as:

$$\begin{cases} L_{inc}(i,\theta) = \dfrac{U_{dc} - 2V_T - Ri_{on}}{di/dt} \\ L_{inc}(i,\theta) = \dfrac{-U_{dc} - 2V_D - Ri_{off}}{di/dt} \end{cases} \tag{6}$$

2.2. Static Initial Drive Phase Estimation

The stator and rotor of the SRM have a double-salient pole structure, and the inductance is highly nonlinear with respect to the rotor position. The rotor position during operation is typically categorized into three forms as illustrated in Fig. 2. At the non-overlapping position, the inductance slope is small, and the phase current is established rapidly. As the rotor approaches the beginning of the overlapping position, the inductance begins to increase, reaching its maximum value when the rotor reaches the overlapping position. The unsaturated inductance characteristics can be obtained through static experiments, with phase A as the reference phase, as shown in Fig. 3(a).

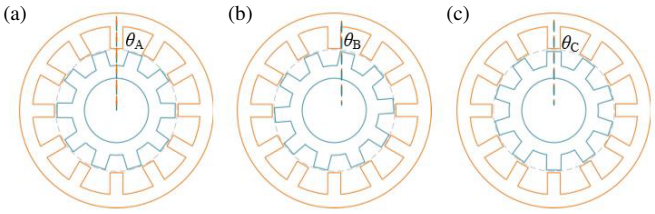

FIGURE 2. The characteristic positions within one cycle. (a) The non-overlapping position. (b) The beginning of the overlapping position. (c) The overlapping position.

The excitation generated by the high-frequency pulse injection method is not sufficient to induce magnetic saturation in the windings, thus resulting in unsaturated inductance. This method is typically used to estimate the initial static phase that is first energized. The inductance distribution of the six-phase SRM is illustrated in Fig. 3(a). The excitation sequence is A-B-C-D-E-F, with a phase separation of 60 electrical degrees. Before starting, high-frequency pulse driving signals are simultaneously applied to all six phases. According to (6), the incremental inductance for each phase can be obtained as L_X, where X = A, B, C, D, E, F. Compared to three-phase and four-phase SRMs, the inductance distribution of six-phase SRM is more densely distributed within one electrical cycle, which increases the difficulty of estimating the initial drive phase. Therefore, this study modifies the control strategy of the six-phase 12/10 SRM to a dual three-phase SRM control strategy. Based on the distribution characteristics of each phase, it is divided into two control groups, namely Group I (A, C, E) and Group II (B, D, F), as shown in Fig. 3(b).

Below is an example estimation of the incremental inductance comparison for Group I. If $L_{\mathrm{A}} > L_{\mathrm{E}}$, phase C is selected as the initial conducting phase; if $L_{\mathrm{E}} > L_{\mathrm{C}}$, phase A is selected as the conducting phase; if $L_{\mathrm{C}} > L_{\mathrm{A}}$, phase E is selected as the conducting phase. Based on the comparison results of the incremental inductance of each phase, one electrical cycle can be divided into regions I–VI, thus completing the selection of conducting phases in different regions. The control strategy of Group II is similar to Group I. Based on this, we have devised Table 1 to display the selection results of the initial drive phase.

2.3. Implementation of High Starting Torque Strategy

Typically, during motor startup, significant output torque is required to overcome inertia, static friction, and load torque. Therefore, after determining the initial drive phase and commutating it, the phase windings are rapidly energized, causing the phase current to exceed the threshold of magnetic saturation, leading the phase into a saturated state. At this moment, there exists a significant discrepancy between the actual inductance and unsaturated inductance, as illustrated in Fig. 4. During position estimation, it is advisable to avoid using saturated

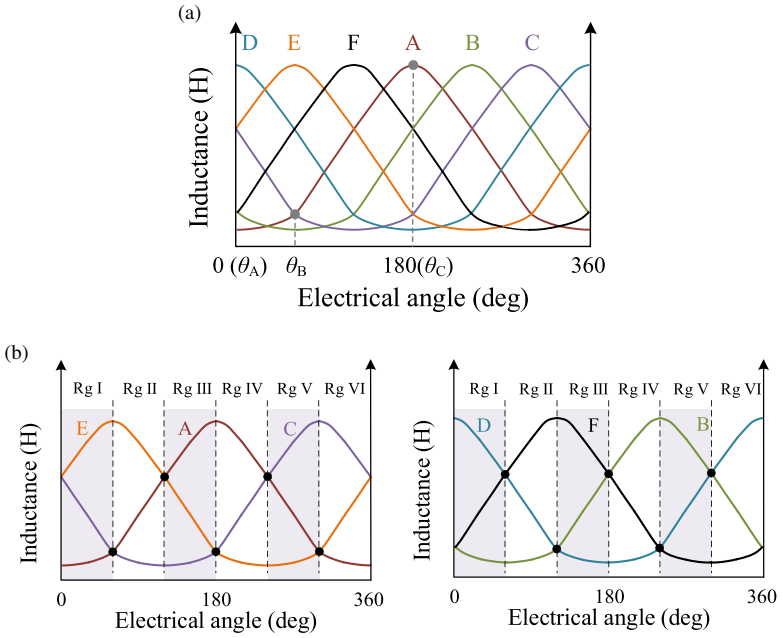

FIGURE 3. The unsaturated inductance characteristics of six phases. (a) Initial state. (b) Grouped state.

inductance due to its strong nonlinear response to current. After designing the initial phase drive, the strategy is to continuously maintain pulse injection on the idle phases. During the initial phase drive process, position information is estimated using the unsaturated inductance of the idle phases. Once the initial drive phase reaches the rotor overlapping position, it is turned off, and after demagnetization, pulse signals are input for position estimation. It is important to note that in order to maintain continuous inductance, pulse signals should be injected once the current in the switched-off phase falls below the saturation current threshold.

Figure 4 illustrates the relationship between phase commutation rules and unsaturated inductance during startup, with similar strategies applied to Group II. Under this strategy, the six-phase SRM maintains at least three-phase conduction, providing significant startup torque.

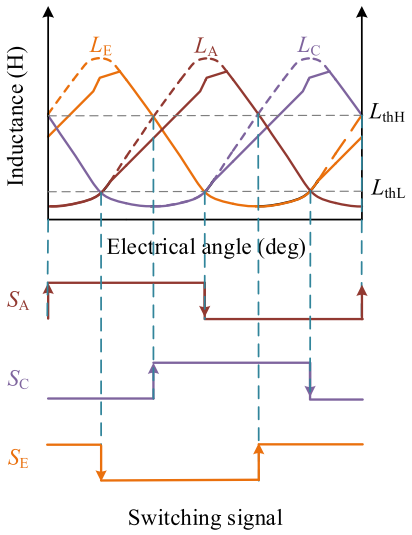

FIGURE 4. The unsaturated inductance characteristics of six phases.

3. POSITION ESTIMATION METHOD BASED ON DYNAMIC INDUCTANCE THRESHOLD

The switching instants of the winding affect the control performance of the speed regulation system. Selecting appropriate angle values can reduce the back EMF effect and improve current tracking performance and torque performance. Therefore, during the control process, the winding is not always conducted for half a period, and reasonable adjustments need to be made according to the operating conditions. This section introduces a dynamic inductance threshold estimation method based on angle adaptivity, further enhancing the performance of the sensorless system.

3.1. Adaptive Switching Angle Planning

In general, advancing the turn-on angle has a weak magnetic field effect, which can reduce the impact of reverse electromotive force and achieve rapid excitation [19]. The selection of the turn-off angle should consider the impact of negative torque, ensuring that the demagnetization process concludes before reaching the rotor overlapping position. Therefore, compared to the startup state, the actual inductance curve during mid-to-low-speed operation will change, as shown in Fig. 5. The timing of winding commutation needs to take into account the changes in operating conditions.

For each phase, the commutation timing within one electrical cycle should follow the same angle rule. The design process of the adaptive commutation angle strategy includes the following steps:

a. The Selection Rule of Turn-on Angle: Real-time adjustment of the commutation angle is achieved through reference

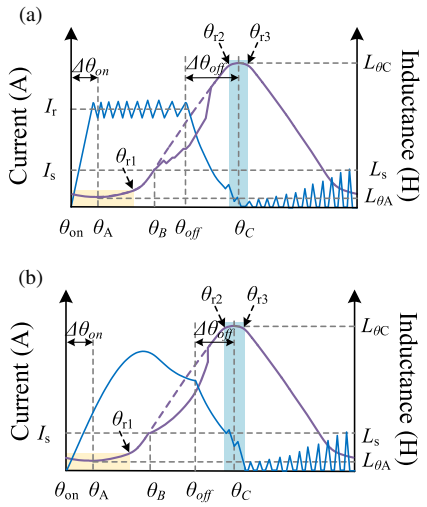

FIGURE 5. Phase inductance characteristic under excitation current. (a) Chopped current control method. (b) Angular position control method.

current detection methods. The phase voltage equation during the excitation stage can be further derived in the form of (7).

$$U_{dc} = 2V_T + Ri + i\omega_{ref}\frac{\partial L_{inc}(i,\theta)}{\partial\theta} + L_{avg}\,\omega_{ref}\frac{di}{d\theta} \tag{7}$$

where ω_{ref} is the reference speed of the SRM, and L_{avg} is the average inductance value of the non-overlapping region.

In practical applications, the phase windings can be rapidly excited in the bottom region of the inductance, with the current rising to the reference value. The inductance slope in this region is very small, and the inductance can be approximated as a constant, i.e., $\frac{\partial L_{inc}(i,\theta)}{\partial\theta} \approx 0$. (7) can be further expressed as:

$$U_{dc} - Ri - 2V_T = L_{avg}\,\omega_{ref}\frac{di}{d\theta} \tag{8}$$

The reference current value is used to calculate the electrical angle traversed by the winding during the excitation process. The boundary of the bottom inductance region is set to the left and right symmetric regions with a distance of $\theta_{r1} - \theta_A$ from the point θ_A. The relationship between the current and rotation angle calculated from (8) is as follows:

$$\theta_{on} = \theta_{ref} - \frac{L_{avg}\,\omega_{ref}}{R}\left(\ln\frac{U - 2V_T}{U - 2V_T - Ri}\right) \tag{9}$$

Increasing the load implies a need for larger phase currents, meaning that the confirmation process for the commutation angle takes into account both the speed and load factors. The leading commutation angle can be calculated as:

$$\Delta\theta_{on} = \theta_A - \theta_{on} \tag{10}$$

It is important to note that the leading value of the commutation angle should be set with a boundary to avoid overshoot.

b. The Selection Rule of Turn-off Angle: At the overlapping position, the unsaturated inductance slope crosses zero in the negative direction. According to the characteristics of SRMs, the output torque is positively correlated with the inductance slope, meaning that the positive or negative slope will result in corresponding positive or negative torque. Near the overlapping position, there exists a region where the inductance changes relatively slowly, as indicated by the areas labeled θ_{r2} and θ_{r3} in Fig. 5. Generally when selecting the turn-off angle, consideration should be given to ensuring that the current can decrease to a certain value within the indicated region. This helps avoid issues such as reduced torque utilization due to excessive leading adjustment and deteriorated torque performance due to excessive lag adjustment, which could arise from large leading or lagging angles [36].

In the optimization process of the turn-off angle, this study adopts the current endpoint detection method proposed by [34], which adjusts the commutation angle adaptively based on the operating conditions. The process is as follows: First is the phase current detection at θ_{r2}. To fully utilize the torque generation capability of the region with a large inductance slope, the phase current at position θ_{r2} should not drop to zero. Taking into account the motor speed and the current at the off time, the adjustment angle at the off time is calculated. The relationship between the lag angle and (i, ω) is similar to an inversely proportional function, and let:

$$\Delta\theta_{off1} = \frac{k_1}{\omega_{ref}\,i_{off}} \tag{11}$$

where $\Delta\theta_{off1}$ is the angle of a delayed turn-off, k_1 a positive coefficient, and i_{off} the current at the turn-off time.

Next is detecting the current at θ_{r3}. If the current is greater than zero, indicating that the demagnetization current exists in the negative inductance slope region, the commutation angle should be advanced at this time to avoid the generation of negative torque. To accelerate the demagnetization process, the leading angle should be chosen as a function that is positively correlated with (i, ω), and let:

$$\Delta\theta_{off2} = k_2\omega_{ref}\,i_{off} \tag{12}$$

where $\Delta\theta_{off2}$ is the angle of advanced off, and k_2 is a negative proportionality coefficient.

Finally, the adjustment angle of the commutation angle can be calculated as:

$$\Delta\theta_{off} = \Delta\theta_{off1} + \Delta\theta_{off2} \tag{13}$$

c. Analysis of the Applicability of the Sensorless Method Proposed Under Determined Conduction Width: Based on the previous description, a conclusion can be drawn that the application of the adaptive commutation strategy results in a reduction in the conduction width of the phase winding within one cycle. Fig. 6 illustrates the conduction rules for Group I under the proposed adaptive threshold strategy, with the control of Group II being consistent with Group I. The turn-on angle is set around the non-overlapping position, where the calculation of inductance coincides with the unsaturated inductance characteristics. This is applicable to the sensorless conduction strategy proposed in the second section and does not introduce errors. Moreover, compared to the conduction strategy during the startup state, the turn-off angle is advanced during adaptive

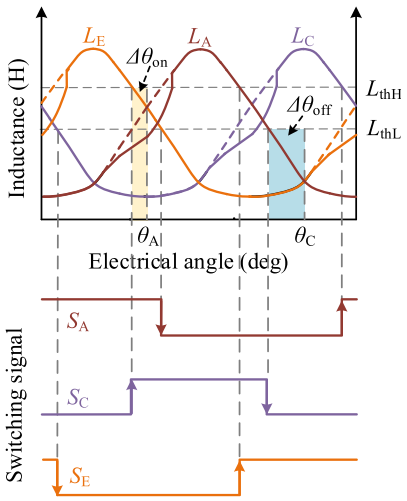

FIGURE 6. Group I conduction rule under the action of the proposed method.

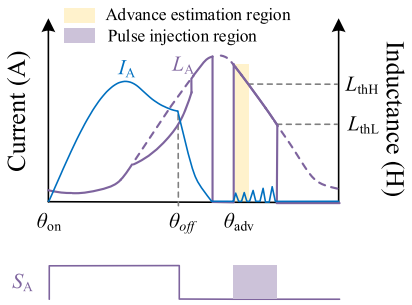

FIGURE 7. Pulse injection optimization method.

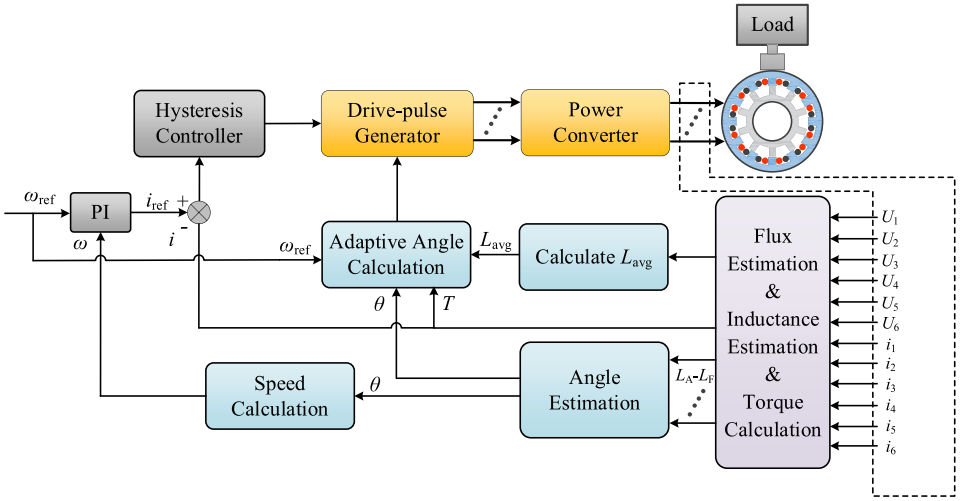

FIGURE 8. Control block diagram in low-to-medium speed operation mode.

adjustment. This allows the estimated phase receiving pulse input to obtain a wider range of unsaturated inductance. Therefore, dynamic inductance thresholds can be chosen over a wider range to achieve a more flexible conduction strategy.

3.2. Idle Phase Pulse Injection Method Optimization

Based on the sensorless conduction strategy designed earlier, targeted optimizations are made to the traditional pulse injection method. In the process of dynamic inductance threshold regulation, the contributing pulse injection region is followed by changes and only needs to be excited in the partially idle stage. The injection of pulses in non-contributing areas not only leads to losses due to the frequent conduction of switching devices but also introduces certain negative torque, thereby reducing torque performance. Therefore, by setting boundaries for the leading edge of the turn-on angle and adjusting the boundaries for the turn-off angle, we apply the pulse injection method selectively in characteristic regions to achieve the estimation of unsaturated inductance. The advantage of this approach lies in its ability to provide the unsaturated inductance characteristics required for position estimation while effectively avoiding the system losses caused by high-frequency pulses. The implementation process is shown in Fig. 7.

Given the anticipation of the leading-on angle reaching the set leading-on boundary value, the starting angle for pulse injection should precede the leading-on boundary by a certain degree to avoid the occurrence of missing calculations for L_{thH}. The unsaturated inductance pre-estimation region is illustrated in the yellow area as depicted in Fig. 7, while the pulse injection region is indicated by the purple-highlighted area. Here, (L_{thH}, L_{thL}) represents the dynamic thresholds associated with $(\theta_{on}, \theta_{off})$.

4. VERIFICATION

To validate the effectiveness of the proposed method for sensorless control, simulations were conducted based on prototype data from a six-phase 12/10 SRM. Fig. 8 illustrates the control logic of the proposed sensorless method at medium-to-low

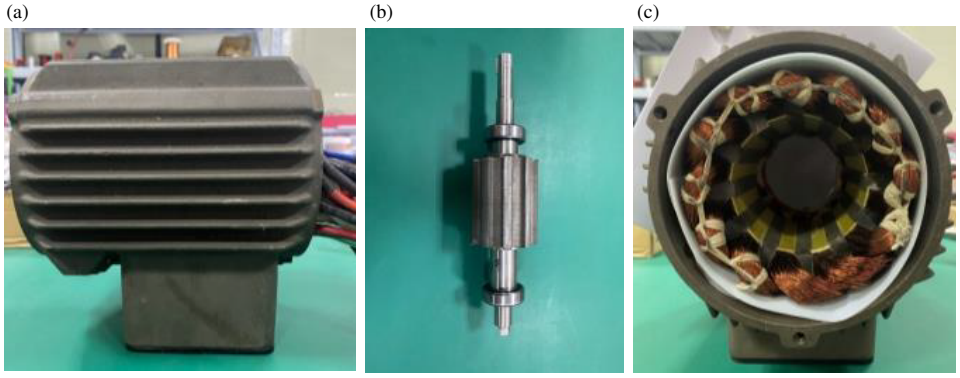

FIGURE 9. Prototype. (a) Motor housing. (b) Rotor. (c) Stator winding.

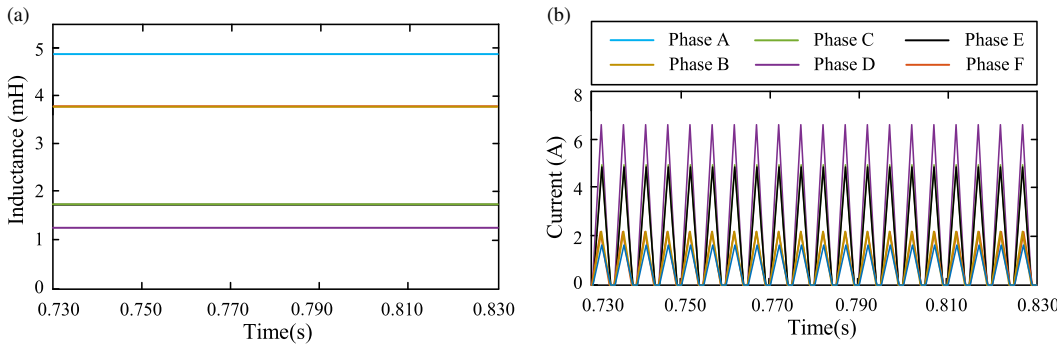

FIGURE 10. Static inductance and current under high frequency pulse injection. (a) Phase inductance. (b) Phase current.

speeds. In the simulation model, current and voltage values are input into the flux and inductance estimation modules, which calculate the inductance, average inductance, and flux linkage. Angle values are reconstructed from the simulated inductance curves, and speed values are obtained by differentiating the angle. The adaptive angle calculation module and current hysteresis control module jointly generate the drive signals for the six-phase power converter. Additionally, the data such as motor flux characteristics and torque characteristics obtained from finite element analysis software are utilized in constructing the motor body module.

Figure 9 illustrates the physical prototype of the machine. The motor parameters are listed in Table 2.

TABLE 2. Parameters of the SRM.

Items	Values
Number of phases	6
Number of stator poles	12
Number of rotor poles	10
Number of turns	15
Outer diameter (mm)	130
Air Gap (mm)	0.4

For the proposed sensorless strategy, determining the startup phase of the motor when it is static is a crucial step. Therefore, a static phase estimation condition is designed. In the initial stage, high-frequency voltage pulses are applied to the six-phase windings, and according to (6), the unsaturated inductance values for the current position are obtained. The simulation results are depicted in Fig. 10. Fig. 10(a) illustrates the six-phase inductance values at static positions, while Fig. 10(b) portrays the current waveforms of the six-phase windings under the influence of high-frequency voltage.

The initial rotor position during the simulation is set to the aligned position of phase A (180°). The unsaturated inductance characteristics of each phase at the 180° position can be obtained from Fig. 3(a). It can be seen that the inductance relationship at this position is: $L_A > L_B = L_F > L_C = L_E > L_D$. During the simulation, high-frequency voltage pulses were applied to the six phases, and the unsaturated inductance results calculated using (6) are shown in Fig. 10(a). From the simulation results, it can be observed that L_A has the largest value; L_B and L_F have approximately equal values and nearly overlap in the simulation result graph; similarly, L_C and L_E are approximately a single line; L_D has the smallest value. It can be seen that at the initial position (180°), the inductance magnitude relationship obtained through simulation calculations is consistent with the inductance characteristics shown in Fig. 3(a). This proves the effectiveness of the inductance calculation method proposed in this paper and the accuracy of the static position estimation.

Figure 11 shows the inductance estimation and signal excitation results for the start-up phase and low-to-medium speed

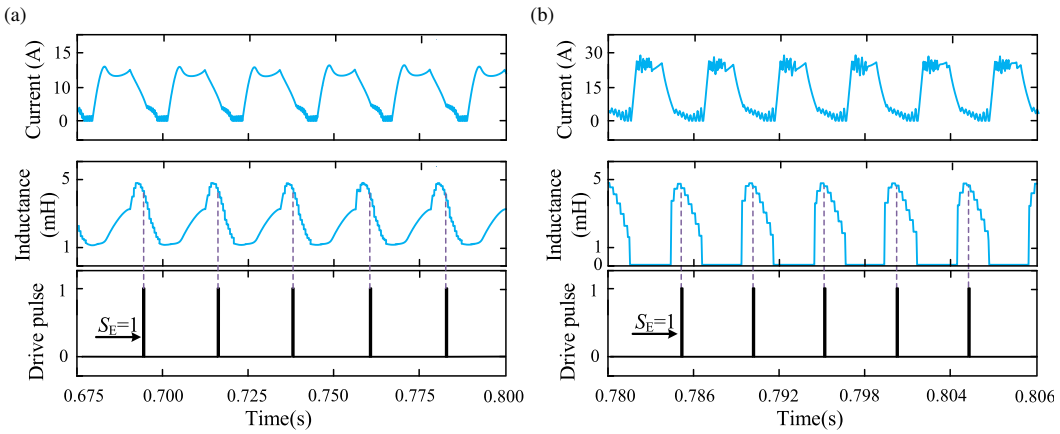

FIGURE 11. Inductance estimation results and excitation signals in start-up and low-to-medium speed. (a) Start-up state. (b) Low-to-medium speed state.

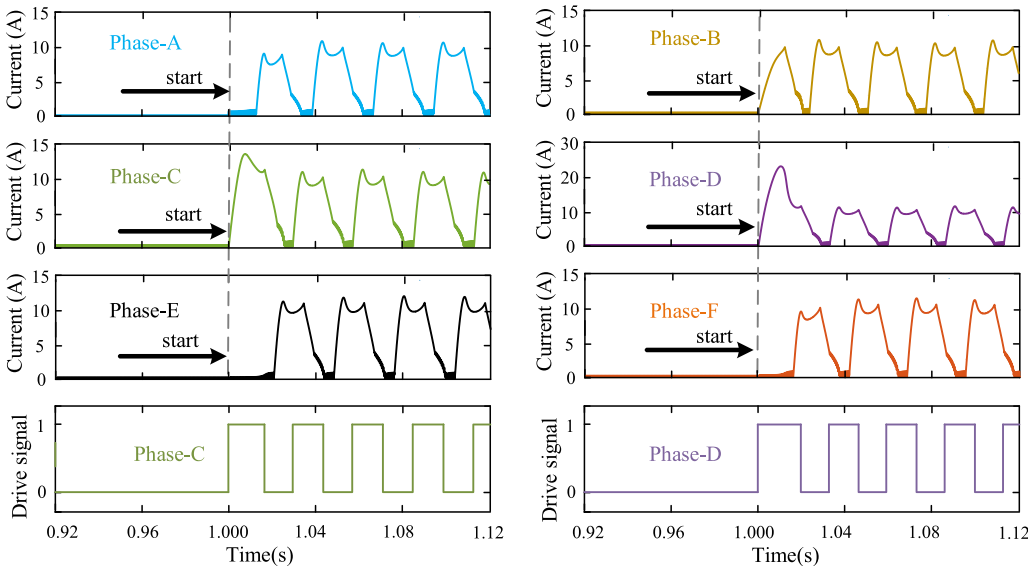

FIGURE 12. Current change and phase excitation signal before and after starting.

phase. In Fig. 11(a), the speed stabilizes at 260 r/min, and the measured current and voltage are used to calculate the inductance over the entire cycle, which is divided into the conduction zone inductance and pulse injection zone inductance. The determination of the opening signal for the corresponding phase is based on the threshold of the inductance in the pulse injection zone. Taking phase A as an example, the pulse is injected from the high inductance threshold point to the conduction of phase E, as shown in the figure. Similarly, Fig. 11(b) presents the simulation results of the sensorless strategy at low-to-medium speed, with the speed stabilized at 1200 r/min. The inductance curve for the pulse injection zone is provided, and the high inductance threshold point of phase A yields the conduction pulse for phase E.

Below is the simulation of the conditions from static detection of the startup phase to the initiation of startup. The results are depicted in Fig. 12, illustrating the waveforms of the six-phase currents and the changes in the conduction signals of phases C and D. Static startup phase confirmation is conducted from 0 s to 1 s. At 1 s, the startup is enabled. According to the static startup rules in Table 1, it can be observed that initially, phases B, C, and D are excited. Therefore, at any given moment during the startup phase, at least three phases are conducted, ensuring the ability for high torque startup. During the excitation signal identification, the six phases are treated as dual three-phase for control purposes. Taking phase C as an example in Group I, the conduction signal of phase C is shown, and the same principle applies to phases A and E. In Group II, phase D is exemplified.

Through a set of comparative experiments, we validate the superior high-torque startup capability of the proposed method. In Fig. 13, with the same input voltage and load torque, the startup capabilities are demonstrated by comparing the speed performance of the two methods. It can be observed that the proposed method stabilizes at approximately 220 r/min, which is higher than the speed of 130 r/min achieved by the traditional dual-phase startup method. Moreover, the proposed method exhibits better stability. Fig. 14 presents the construction re-

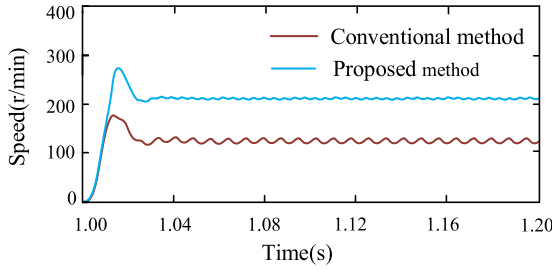

FIGURE 13. The comparison of starting ability of the two methods under the same voltage and load.

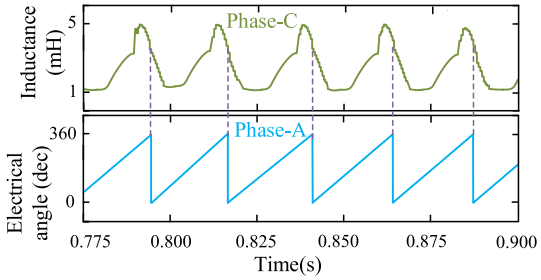

FIGURE 14. The results of the electrical angle construction of the proposed method.

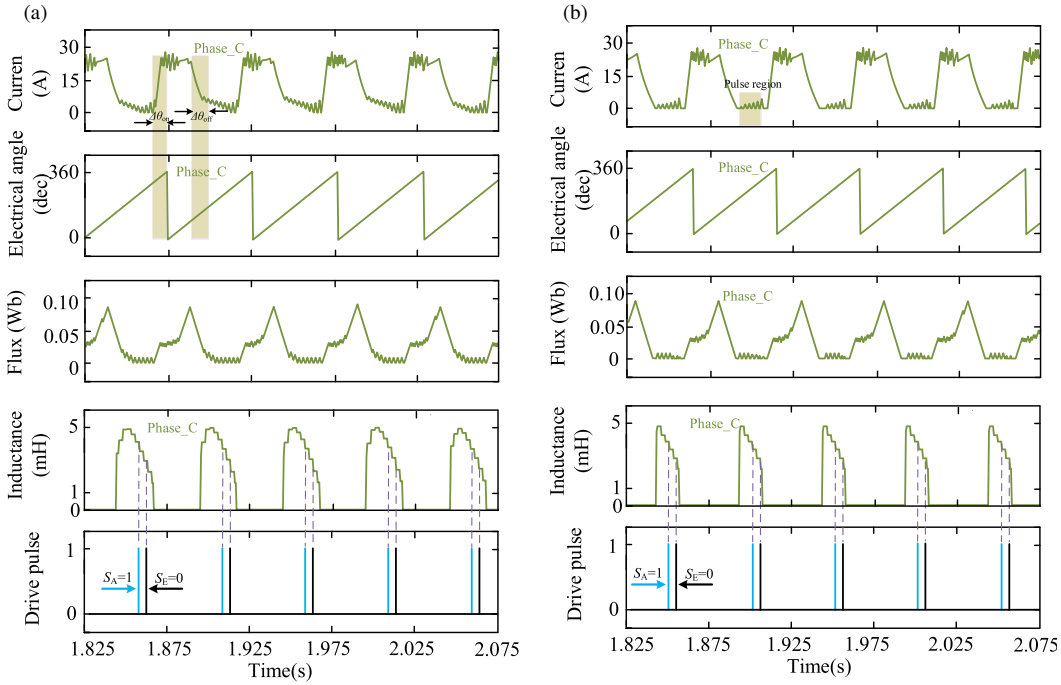

FIGURE 15. Comparison of the results of two pulse injection methods. (a) Traditional method. (b) Optimization method.

TABLE 3. Comparison between the proposed method and the traditional method.

Methods	Prior model data	Computation complexity	Application stages	Magnetic saturation effect	Adjustable conduction width
Method of [21]	Yes	Yes	Full speed	Yes	No
Method of [22]	Yes	Yes	Full speed	Yes	No
Method of [23]	Yes	Yes	Full speed	Yes	Yes
Method of [26]	No	No	Low speed	No	No
Method of [27]	No	No	Full speed	Yes	No
Method of [28]	No	Yes	Low speed	No	No
Proposed method	No	No	Medium-low speed	No	Yes

sults of the full electrical angle of phase A based on inductance threshold identification.

Simulation scenarios are designed to validate the effectiveness of the idle-phase pulse injection optimization method. Fig. 15(a) depicts the simulation results of the traditional idle-phase pulse injection method, where $\Delta\theta_{on}$ represents the leading-on angle obtained using the adaptive angle tuning method, and $\Delta\theta_{off}$ is the leading-off angle for early winding cutoff to prevent undesired negative torque. Fig. 15(b) presents the simulation results of the optimized idle-phase pulse injection method. It can be observed that, based on the adaptive angle tuning, the pulse injection region has been adjusted

effectively, reducing the pulse injection time and mitigating the switch losses caused by frequent conduction. Furthermore, the modified pulse injection region still encompasses the required inductance threshold, ensuring that the excitation pulses for other phases remain unaffected.

For the initial position detection, start-up phase, and medium-low-speed operation, a complete simulation process is shown in Fig. 16. It presents the rotor speed curve and phase current curves for phases (A, C, E) and similar current situations for phases (B, D, F). During this process, the start signal is enabled at 0.3 s. At 0.8 s, the system switches to a medium-low-speed strategy with a set speed of 1000 r/min. Finally, at 1.3 s, a speed step change is applied, increasing the set speed to 1500 r/min. From the simulation results, it is evident that the system can smoothly follow the reference speed command and achieve stability.

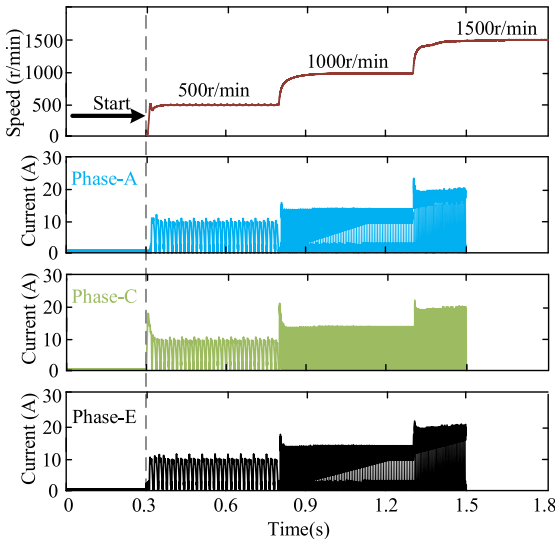

FIGURE 16. Complete speed regulation process of the proposed method.

The systematic comparison of the proposed method with the typical traditional sensorless starting methods is presented in Table 3.

5. CONCLUSION

This paper proposes a sensorless control strategy applicable during startup and low-to-medium speed operation. By formulating a conduction strategy for the static startup, the high-torque startup capability is enhanced. Moreover, based on the electromagnetic characteristics of the SRM, an adaptive angle adjustment module is designed to optimize the conduction width of phases, fully maximizing the excitation capability of the phases and effectively avoiding the occurrence of negative torque. Considering the influence of the AHB circuit and the voltage drop across the windings, the unsaturated inductance calculation model is improved to enhance the accuracy of inductance calculation. The effectiveness and accuracy of the proposed method are validated through simulation on a 6-phase 12/10 SRM prototype.

REFERENCES

[1] Feng, L., X. Sun, Z. Yang, and K. Diao, "Optimal torque sharing function control for switched reluctance motors based on active disturbance rejection controller," *IEEE/ASME Transactions on Mechatronics*, Vol. 28, No. 5, 2600–2608, Oct. 2023.

[2] Zaghari, B., A. Stuikys, A. S. Weddell, and S. Beeby, "Efficient energy conversion in electrically assisted bicycles using a switched reluctance machine under torque control," *IEEE Access*, Vol. 8, 202 401–202 411, 2020.

[3] Feng, L., X. Sun, G. Bramerdorfer, Z. Zhu, Y. Cai, K. Diao, and L. Chen, "A review on control techniques of switched reluctance motors for performance improvement," *Renewable and Sustainable Energy Reviews*, Vol. 199, 114454, 2024.

[4] Chiba, A., K. Kiyota, N. Hoshi, M. Takemoto, and S. Ogasawara, "Development of a rare-earth-free SR motor with high torque density for hybrid vehicles," *IEEE Transactions on Energy Conversion*, Vol. 30, No. 1, 175–182, Mar. 2015.

[5] Sun, X., Y. Wen, L. Zhang, M. Yao, and G. Lei, "Fault detection and fault-tolerant control of switched reluctance motor based on dual-sensor current detection scheme," *IEEE Transactions on Transportation Electrification*, 2024.

[6] Panda, D. and V. Ramanarayanan, "Reduced acoustic noise variable DC-bus-voltage-based sensorless switched reluctance motor drive for HVAC applications," *IEEE Transactions on Industrial Electronics*, Vol. 54, No. 4, 2065–2078, Aug. 2007.

[7] Khalil, A., S. Underwood, I. Husain, H. Klode, B. Lequesne, S. Gopalakrishnan, and A. M. Omekanda, "Four-quadrant pulse injection and sliding-mode-observer-based sensorless operation of a switched reluctance machine over entire speed range including zero speed," *IEEE Transactions on Industry Applications*, Vol. 43, No. 3, 714–723, 2007.

[8] Cai, Y., Y. Wang, H. Xu, S. Sun, C. Wang, and L. Sun, "Research on rotor position model for switched reluctance motor using neural network," *IEEE/ASME Transactions on Mechatronics*, Vol. 23, No. 6, 2762–2773, Sep. 2018.

[9] Sun, X., N. Wang, Y. Cao, D. Guo, M. Yao, Y. Sun, and Y. Xiong, "Nonlinear fast modeling method of flux linkage and torque for a 12/8 switched reluctance motors," *IEEE Transactions on Power Electronics*, Vol. 39, No. 5, 5298–5309, May 2024.

[10] Hudson, C. A., N. S. Lobo, and R. Krishnan, "Sensorless control of single switch-based switched reluctance motor drive using neural network," *IEEE Transactions on Industrial Electronics*, Vol. 55, No. 1, 321–329, Jan. 2008.

[11] Sun, X., X. Tang, X. Tian, J. Wu, and J. Zhu, "Position sensorless control of switched reluctance motor drives based on a new sliding mode observer using fourier flux linkage model," *IEEE Transactions on Energy Conversion*, Vol. 37, No. 2, 978–988, Jun. 2022.

[12] Kim, J.-H. and R.-Y. Kim, "Sensorless direct torque control using the inductance inflection point for a switched reluctance motor," *IEEE Transactions on Industrial Electronics*, Vol. 65, No. 12, 9336–9345, Dec. 2018.

[13] Song, S., S. Chen, and W. Liu, "Analytical rotor position estimation for SRM based on scaling of reluctance characteristics from torque-balanced measurement," *IEEE Transactions on Industrial Electronics*, Vol. 64, No. 5, 3524–3536, May 2017.

[14] Sun, Q., T. Lan, X. Liu, S. Li, F. Niu, and C. Gan, "Linear inductance model reshaping-based sensorless position estimation method for SRM with anti-magnetic saturation capability," *IEEE Journal of Emerging and Selected Topics in Power Electronics*, Vol. 11, No. 5, 4799–4807, Oct. 2023.

[15] Sun, X., N. Wang, M. Yao, and G. Lei, "Position sensorless control of SRMs based on improved sliding mode speed controller and position observer," *IEEE Transactions on Industrial Electronics*, 1–11, 2024.

[16] Yalavarthi, A. and B. Singh, "An adaptive-gain super-twisting position observer for grid-interfaced SRM water pump," *IEEE Transactions on Consumer Electronics*, Vol. 68, No. 4, 366–375, Nov. 2022.

[17] Yalavarthi, A. and B. Singh, "SMO-based position sensorless SRM drive for battery-supported PV submersible pumps," *IEEE Journal of Emerging and Selected Topics in Power Electronics*, Vol. 10, No. 4, 3917–3926, Aug. 2022.

[18] Sun, X., Y. Zhu, Y. Cai, M. Yao, Y. Sun, and G. Lei, "Optimized-sector-based model predictive torque control with sliding mode controller for switched reluctance motor," *IEEE Transactions on Energy Conversion*, Vol. 39, No. 1, 379–388, Mar. 2024.

[19] Feng, L., X. Sun, D. Guo, M. Yao, and K. Diao, "Advanced torque sharing function strategy with sliding mode control for switched reluctance motors," *IEEE Transactions on Transportation Electrification*, Vol. 10, No. 1, 2302–2311, Mar. 2024.

[20] Ye, J., B. Bilgin, and A. Emadi, "Elimination of mutual flux effect on rotor position estimation of switched reluctance motor drives considering magnetic saturation," *IEEE Transactions on Power Electronics*, Vol. 30, No. 2, 532–536, Feb. 2015.

[21] Kumar, A., B. Singh, and G. Singh, "MPC based position sensorless SRM drive for light electric vehicles with optimized voltage vectors and reduced torque ripple," *IEEE Transactions on Industry Applications*, Vol. 60, No. 2, 3237–3246, Mar.-Apr. 2024.

[22] Kumar, A., B. Singh, and G. Singh, "Modified direct torque control of solar fed sensorless switched reluctance motor drive for electric vehicle with regenerative braking," *IEEE Transactions on Industry Applications*, Vol. 60, No. 2, 3155–3164, Mar.-Apr. 2024.

[23] Sun, X., N. Wang, M. Yao, and G. Lei, "Position sensorless control of switched reluctance motors based on angle adjustment using nonlinear inductance and flux model," *IEEE Transactions on Industrial Electronics*, 1–11, 2024.

[24] Shen, L., J. Wu, and S. Yang, "Initial position estimation in SRM using bootstrap circuit without predefined inductance parameters," *IEEE Transactions on Power Electronics*, Vol. 26, No. 9, 2449–2456, Sep. 2011.

[25] Pasquesoone, G., R. Mikail, and I. Husain, "Position estimation at starting and lower speed in three-phase switched reluctance machines using pulse injection and two thresholds," *IEEE Transactions on Industry Applications*, Vol. 47, No. 4, 1724–1731, Jul. 2011.

[26] Cai, J., Y. Yan, W. Zhang, and X. Zhao, "A reliable sensorless starting scheme for SRM with lowered pulse injection current influences," *IEEE Transactions on Instrumentation and Measurement*, Vol. 70, 1–9, 2020.

[27] Cai, J., Z. Liu, and Y. Zeng, "Aligned position estimation based fault-tolerant sensorless control strategy for SRM drives," *IEEE Transactions on Power Electronics*, Vol. 34, No. 8, 7754–7762, Aug. 2019.

[28] Cai, J., X. Zhang, X. Peng, Y. Yan, and Z. Deng, "A hybrid sensorless starting strategy for SRM with fault-tolerant capability," *IEEE Transactions on Transportation Electrification*, Vol. 9, No. 2, 2444–2452, Jun. 2023.

[29] Fang, G., F. P. Scalcon, C. J. V. Filho, D. Xiao, B. Nahid-Mobarakeh, and A. Emadi, "A unified wide-speed range sensorless control method for switched reluctance machines based on unsaturated reluctance," *IEEE Transactions on Industrial Electronics*, Vol. 70, No. 10, 9903–9913, Oct. 2023.

[30] Sun, X., Y. Zhu, Y. Cai, Z. Zhu, and Y. Xiong, "Speed sensorless control of switched reluctance motors in full speed range based on inductance characteristics," *IEEE Transactions on Transportation Electrification*, Vol. 10, No. 2, 4018–4028, Jun. 2024.

[31] Bateman, C. J., B. C. Mecrow, A. C. Clothier, P. P. Acarnley, and N. D. Tuftnell, "Sensorless operation of an ultra-high-speed switched reluctance machine," *IEEE Transactions on Industry Applications*, Vol. 46, No. 6, 2329–2337, Nov.-Dec. 2010.

[32] Gribble, J. J., P. C. Kjaer, and T. J. E. Miller, "Optimal commutation in average torque control of switched reluctance motors," *IEE Proceedings — Electric Power Applications*, Vol. 146, No. 1, 2–10, Jan. 1999.

[33] Hwu, K. I. and C. M. Liaw, "Intelligent tuning of commutation for maximum torque capability of a switched reluctance motor," *IEEE Transactions on Energy Conversion*, Vol. 18, No. 1, 113–120, Mar. 2003.

[34] Sun, Q., J. Wu, and C. Gan, "Optimized direct instantaneous torque control for SRMs with efficiency improvement," *IEEE Transactions on Industrial Electronics*, Vol. 68, No. 3, 2072–2082, Mar. 2021.

[35] Kim, J. and J.-S. Lai, "Quad sampling incremental inductance measurement through current loop for switched reluctance motor," *IEEE Transactions on Instrumentation and Measurement*, Vol. 69, No. 7, 4251–4257, Jul. 2020.

[36] Xu, Y. Z., R. Zhong, L. Chen, and S. L. Lu, "Analytical method to optimise turn-on angle and turn-off angle for switched reluctance motor drives," *IET Electric Power Applications*, Vol. 6, No. 9, 593–603, Nov. 2012.